Hindawi
International Journal of Energy Research
Volume 2024, Article ID 2138847, 18 pages
https://doi.org/10.1155/2024/2138847

WILEY | Hindawi

Research Article

Phonon DOS-Based Machine Learning Model for Designing High-Performance Solid Electrolytes in Li-Ion Batteries

Russlan Jaafreh,[1] Santiago Pereznieto,[1] Seonghun Jeong,[2] I. Putu Widiantara,[3] Jeong Moo Oh,[3] Jee-Hyun Kang,[3] Junyoung Mun,[2] Young Gun Ko,[3] Jung-Gu Kim,[4] and Kotiba Hamad[1]

[1]*Material's Automated Design & Discovery Lab, School of Advanced Materials Science & Engineering Sungkyunkwan University, Suwon 16419, Republic of Korea*
[2]*Laboratory for Advanced Batteries, School of Advanced Materials Science & Engineering Sungkyunkwan University, Suwon 16419, Republic of Korea*
[3]*School of Materials Science and Engineering, Yeungnam University, Gyeongsan 38541, Republic of Korea*
[4]*Applied Electrochemistry Lab, School of Advanced Materials Science & Engineering Sungkyunkwan University, Suwon 16419, Republic of Korea*

Correspondence should be addressed to Young Gun Ko; kotibahamad995@gmail.com, Jung-Gu Kim; kimjg@skku.edu, and Kotiba Hamad; hamad82@skku.edu

Received 30 August 2023; Revised 26 October 2023; Accepted 29 December 2023; Published 24 January 2024

Academic Editor: Raja Sen

In the present work, a machine learning (ML) model was built to design solid electrolytes with improved ionic conductivity for Li-ion batteries (LIBs), and the model was based on the phonon density of states (PhDOS). Compounds with PhDOS calculations were collected from the Materials Project (MP) and processed to obtain frequencies and PhDOS to calculate the total phonon band center, a proxy for ionic conductivity. Total phonon band centers were involved in a learning process using four ML algorithms (extra random trees (XT), gradient boosting (GB), extreme gradient boosting (XGB), and decision trees (DT)). The cross-validation results from the algorithms showed that the performance of the XT-model was superior and confirmed through density functional theory- (DFT-) based phonon calculations conducted on $LiYO_3$, Li_4CO_4, $LiNiO_3$, $LiGeO_3$, and $LiSiO_3$. The XT-model was then used to predict the total phonon band centers of new compounds where these had no phonon calculations beforehand. Experimental validation of the XT-model involved electrochemical impedance spectroscopy (EIS) measurements on two compounds: Li_2CO_3 from the high range and Li_6PS_5Cl from the low range. Additionally, $LiBiO_2$ that is predicted to have low total phonon band center, according to the XT-model, was considered further to estimate its potential as solid electrolyte in LIBs.

1. Introduction

Lithium-ion batteries (LIBs) have been around for the last four decades with their popularity still increasing as they are being manufactured more than ever [1]. LIBs are important because they offer better performance both in their charging and discharging states as they have higher efficiency and lower environmental impact than their lead-acid predecessors. For now, the cost of lithium batteries is higher than lead-acid ones; however it has been rapidly decreasing since their invention forty years ago.

The most important components in these batteries are the electrodes (cathode and anode) and the electrolyte, which is the substance that allows ion movement from one electrode to another. Current LIBs employ a liquid electrolyte; however, this can be hazardous due to its flammability when exposed to oxygen [2], or in the case of leakage, their contents can cause chemical burns and other severe

complications [2]. Corrosion is another significant disadvantage with liquid electrolytes since they can corrode the surrounding materials inside the battery and cause a decrease in performance and overall safety [3].

To address liquid electrolyte drawbacks in conventional LIBs, solid-state batteries (SSBs) use safer solid electrolytes, reducing leakage and ignition risks while offering higher energy density [4]. Additionally, these electrolytes exhibit lower discharge rates, promoting longer operation, and environmental friendliness by employing ceramics or polymers [4], which are more sustainable and less toxic than their liquid counterparts. Polymer electrolytes, being nonflammable and mechanically stable, offer advantages over liquid counterparts but face limitations due to their lower ionic conductivity and issues like degradation and moisture adsorption in the polymer matrix, requiring optimization for performance in polymer electrolyte LIBs [5].

Ceramic electrolytes, including oxide-, halide-, and sulfide-based materials, outperform polymer electrolytes with higher ionic conductivity, thermal stability, and mechanical strength [6]. They hold promise for LIB industry adoption after extensive research. Focus lies on enhancing toughness due to ionic bonding-induced brittleness, improving electrochemical stability with electrodes, and boosting ionic conductivity compared to liquid electrolytes [7–9]. Some ceramic electrolytes match $LiPF_6$ (the most commonly used liquid electrolyte) [10] in ionic conductivity, such as NASICON (sodium super ionic conductors) [11–13], LISICON (lithium super ionic conductors) [14, 15], Garnet-type solid electrolytes [16], perovskites [17], argyrodites [18], and others [19, 20]. Notably, ionic conductivity can be adjusted through structural modifications; e.g., LGPX ($Li_{10}GeP_2X_{12}$), which belongs to the LISICON group, exhibits enhanced conductivity when moving from X=O to Se, linked to reduced activation energy and increased crystal volume for Li-ion diffusion [21].

Up to here, considering their superior properties over other types of solid and liquid electrolytes, it is worthwhile to think of enhancing the ionic conductivity of ceramic-based electrolytes, to increase their applicability in solid-state LIBs. Searching for new materials that might show higher performance as compared to on-hand materials can be mainly done through experimental procedures. However, atomistic modeling, such as the density functional theory (DFT) [22] and molecular dynamics (MD) [23], can also be employed relatively successfully to simulate the behavior of the new materials at atomistic levels. Both the experimental procedures and simulations are time-consuming and costly, and they are mostly not suitable for large-scale discovery processes. As a complementary step forward, artificial intelligence (AI) techniques, like machine learning (ML) and deep learning (DL), can be utilized, where these techniques have been increasingly imbedded as an indispensable tool in the field of automated materials discovery in recent years [24]. Such techniques can quickly sift through vast amounts of data and identify patterns that would be difficult for humans to detect, which significantly reduces the complicated and time-consuming simulations and experimental procedures. The high potential of AI in the field of materials discovery is largely due to the vast amount of knowledge accumulated in this field over many years of traditional research. In addition, the development in computing hardware and AI algorithms opens the door widely in employing AI techniques in various fields, including materials science and engineering. Indeed, intensive research was reported on the employment of AI to predict the materials' performance for various applications, such as thermal transport properties such as lattice thermal conductivity and thermal figure of merit [25–27]. In our previous work, ML algorithms were employed to build models that can predict the ionic conductivity of electrolytes in a wide range of temperatures [28]. The models were built using manually collected data from other works reported on the preparation and characterization of solid electrolytes for Li batteries. Even though the obtained results were interesting in terms of accuracy, there were two limitations in that work. First is that the parameters used to describe the material were based on chemical compositions alone, meaning that the crystal information was not taken into account, and accordingly, the built models had no capability in distinguishing between polymorphous materials, such as diamond and graphite for instance. More importantly, the data included in that work were collected from the literature, where enough information on the processing conditions and related microstructure characteristics was hard to come by, even though they play a major role in determining the overall performance. The present work is designed to address such limitations, where the AI models are built based on both the composition and crystal features only, leading finally to a model that can distinguish between polymorphous materials. In addition, the dataset used in the present work is extracted from open-source material databases, which can provide a wealth of data that can be used to train the models; furthermore, basing our dataset on an open database eliminates the need to concern ourselves with processing parameters and their uniformity at all; namely, through this process, we are trying to construct a model that deals exclusively with a pure single crystal materials with no regard to its processing history or experimental procedures and variables that highly influence their performance. Indeed, this method has its shortcomings when applied to real-world applications and experimental procedure; however it allows us to, as mentioned earlier, sift through thousands of promising, truly novel, materials yielding a more robust modeling architecture and a rapid verification environment overall. Up to here, it is imperative to investigate two works reported by Kong et al. [29] and Chen et al. [30] in relation to the differences and similarities between those and this work. In particular, those specific works deal with establishing predictive models that are more catered towards the total continuous prediction of density of state (phonon and electron) values at different frequencies, while the current work streamlines the phonon density of states to a singular value called the "total phonon band center" which will be expanded upon later. Additionally, the current and aforementioned works employ crystal structure features alongside the composition of the material as well; however, the technique for generating and employing those features

differs greatly in their generation, usage, and interpretation as will be illustrated in later sections. All in all, this work utilizes the combination of open-source material databases and AI techniques that enables faster and more accurate material discovery and optimization in comparison to traditional methodology in material modeling. In the present work, accordingly, the AI techniques will be used to guide the design of new ceramic-based electrolytes with improved ionic conductivity for Li-ion batteries.

2. Learning Procedure

2.1. The Proxy of Phonon Band Center and the Relation to Ionic Conductivity. To build an accurate and reliable ML model that can predict the ionic conductivity characteristics of ceramic-based electrolytes, uniform data should be used in the learning process; if the ionic conductivity was set as a direct output in the model, then the data uniformity will be an issue. Uniformity here refers to the type of information that can be attained for a specific electrolyte material from traditional sources; for instance, some parameters refer to the synthesis of the material, processing conditions, and polycrystalline characterization such as grain boundaries and defects. Usually, such parameters are experimentally measured, and thus, it will be impossible to find uniform processing conditions for enough amount of data. In this regard, to find promising solid electrolyte materials and structures for Li-ion batteries using ML, rather than a direct property (ionic conductivity), a representative proxy can be utilized to relate the targeted property and structure (composition and crystal). Based on the previous example given for the LGPX [21], the crystal volumes of the $Li_{10}GeP_2O_{12}$ and $Li_{10}GeP_2S_{12}$ crystals were used to find the difference in their performance and then to describe their ionic conductivities. Even though the crystal volume performs well in reflecting the ionic conductivity in these two electrolytes, it would be ineffective in describing and comparing solid-state electrolytes from different crystal families. Accordingly, a more general proxy will be needed, to generalize and standardize a reliable method that can be applicable for various families and structures. Here, lattice dynamics and their properties were found to relate to Li-ion mobility within crystals, as reported by Muy et al. [31], who investigated the relationship between the phonon density of states (PhDOS) and energy barriers for Li-ion migration of certain electrolytes. The results showed that the total phonon band center is a singular value that can be determined from the PhDOS according to the following equation [31]:

$$\omega_{\text{av}} = \frac{\int \omega \times \text{DOS}(\omega) d\omega}{\int \text{DOS}(\omega) d\omega}, \tag{1}$$

where ω_{av} is the total phonon band center, ω is the frequency, and $\text{DOS}(\omega)$ is the total phonon DOS, which can be used to qualitatively represent the ionic conductivity of solid electrolytes in Li-ion batteries. The main assumption for this finding was based on the Einstein model [32], which relates the amplitude of the thermal displacement of a chemical species from its equilibrium position (u) in the crystal and phonon frequency (ω) as follows:

$$\left\langle |u|^2 \right\rangle = \frac{3k_B T}{m\omega^2}, \tag{2}$$

where k_B, T, and m are the Boltzmann constant, temperature, and mass of the chemical species, respectively. According to this model, at a specific temperature, the smaller phonon frequency is associated with a higher mobility, where for such a low frequency, the chemical species can oscillate away from its equilibrium position. On the other hand, the high activation energy of migration (less mobility) is associated with the oscillation close to the equilibrium position (high frequency). This hypothesis was supported by the conclusion reached by Wakamura [33] which mentions that the energy barriers of migration in Ag^+, Na^+, and Cu^{2+} conductors decrease with decreasing phonon frequency in the optical mode [33], confirming the relationship between the phonon frequency and the probability of a chemical species to leave its position into a neighboring one. Additionally, this was investigated on number of Li-ion conductors including Li_4SnS_4, Li_4GeS_4, Li_3PS_4 (*Pnma*), Li_3PS_4 ($Pmn2_1$), Li_4GeS_4 (*Cmcm*), Li_3VO_4, Li_3PO_4 (*Pnma*), and Li_3PO_4 ($Pmn2_1$), as reported by Muy et al. [31], where the obtained results supported this hypothesis. It was experimentally found that replacing O in Li_3PO_4 ($Pmn2_1$) by S will lead to a softening in this so-called total phonon band center and a decrease in the activation energy from 1.4 eV in Li_3PO_4 to 0.5 eV in Li_3SO_4. Other results reported by the same group [29] on the relationship between the total phonon band center and the measured activation energy are shown in Figure 1(a).

2.2. Learning Data. The initial dataset used in the learning process of this work were collected from the Materials Project (MP) database [34], where the compounds (~1272) alongside their PhDOS calculations (frequency and DOS) were collected, and among them, 114 were Li-containing compounds, such as $LiSbF_6$. The data including PhDOS and frequency for each compound were obtained from MP (an example is given in Figure 1(b)), and the total phonon band center of these compounds was estimated using Eq. (1) (more information about the methodology is given in the supplementary materials and Figure S1). The distribution of the estimated values of the total phonon band centers for these compounds is presented in Figure 1(b). It can be noted that the values are distributed between 5 to ~120 meV and between 15 to 78 meV for the Li-containing compounds. In addition, most of these compounds were oxide-based, and a majority of the overall data had a cubic crystal structure, as shown by Figures 1(c) and 1(d), respectively. Accordingly, O is the most contributing element in these compounds followed by K, F, P, and S, as shown by the heatmap of the element contributions in Figure 1(e). Such distribution in the initial dataset, which is going to be used for the learning process in this work, can result in a ML model with a wide window of predictability, wherein a confident decision can be taken on whether a material is expected to show a

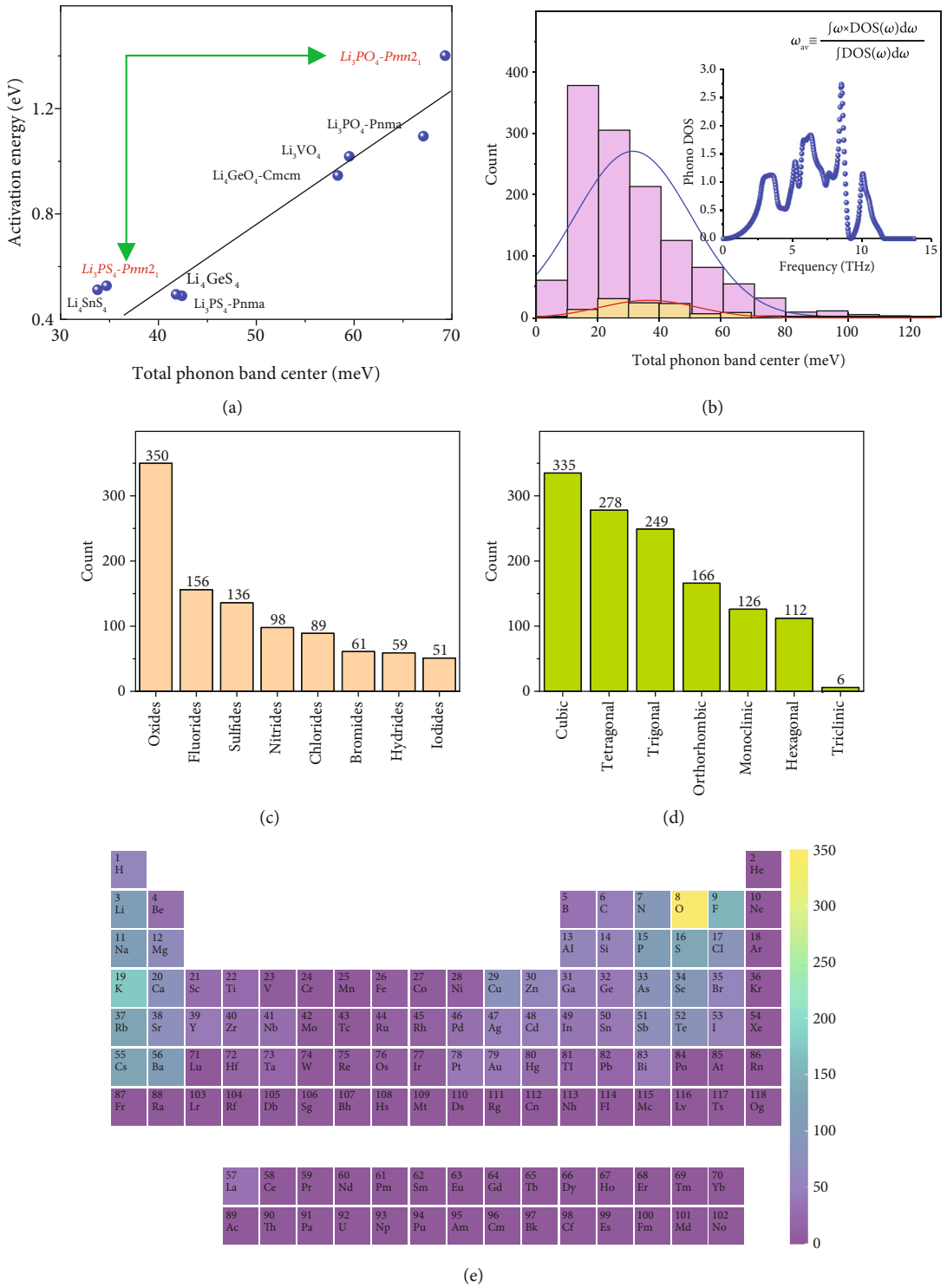

FIGURE 1: The characteristics of the data used in the present learning process. (a) The relationship between the total phonon band center and the activation energy related to the diffusion of Li ions in some compounds including Li_3PO_4 ($Pmn2_1$), Li_3PS_4 ($Pmn2_1$), Li_3PO_4 ($Pnma$), Li_3SO_4 ($Pnma$), Li_4GeO_4 ($Cmcm$), Li_3VO_4, Li_4GS_4 ($Cmcm$), and Li_4SnS_4 [31]. The activation energy is the summation of energy needed to generate vacancies and the migration energy of Li ions. (b) The histogram of the total phonon band centers, which are determined from the PhDOS diagrams (one example is embedded in this figure) of the compounds included in the initial dataset. The highlighted histogram in (b) is related to the Li-containing compounds (114 compounds) in this dataset. (c, d) The distribution of the compounds used in the initial dataset based on their type and crystal system, respectively, where most of the compounds are oxide-based and most materials possess a cubic crystal structure. (e) A heatmap of the periodic table to visualize the contribution of the elements in the compounds used in the initial dataset, showing that among all elements, O had the most contribution in the included compounds.

relatively high performance as a solid electrolyte in Li-ion batteries in general.

2.3. Feature Engineering. Once the initial dataset is collected, the following step is to generate a set of material descriptors, called features that quantitatively describe the materials that we have collected as well as the materials to be generated further for validation processes. The feature generation process is indeed a very interesting topic on its own, and there are numerous ways to represent a material according to the scale of the intended representation. In this work, we have opted to use a feature generation method that depends both on the chemical composition and the crystal structure of the representative unit cell of the compound. Ward et al. [35, 36] have developed a proprietary framework, the Materials agnostic platform for informatics and exploration (Magpie), that can help accelerate and standardize the feature generation process for materials in both their composition and crystal structures alike. This process has been used in previous works for brittle and ductile characterization of Mg-based materials [37], superhard materials [38], and perovskite stability prediction [39]. Multiple other feature generation methodologies such as the Smooth Overlap of Atomic Positions (SOAP), which provides descriptors of the local geometries using a Gaussian smeared atomic density [40], and the Ewald Sum Matrix (ESM), which generates features that relate to the positional environment of the electrostatic interactions between the atoms in a material [41], are indeed used to generate unique and useful features for the compositional content and crystal structure configuration of materials, yet they are, as have been shown by in a previous work [39], computationally extensive, by generating a huge number of features for each material (>1 k features), and redundant by using a huge number of padded features according to the largest unit cell in the dataset overall, which is required for all materials to possess the same number of features for the training and testing. Circling back to the works by Chen et al. [29] and Kong et al. [30], those, similarly, allow a more extensive description of the crystal structure by embedding the crystal structures to an encoder algorithm that maps scalar features to different positions in the unit cell that is being under investigation, which are modified variations of the Euclidean Neural Networks (E3NN) [42] and the Graph Convolutional Networks with global attention (GATGNN) [43] frameworks of crystal features encoding. Yet, and as discussed in a previous work [39], the use of those features is highly sensitive to the initial unit cell size and initial parameters used to set the cutoffs relating to the effects of atoms and their neighboring environments. This problem is in fact mitigated by Ward et al. [35, 36] in their Magpie platform, by segmenting the structure of a specific compound according to the Voronoi Tessellation algorithm [44], resulting in a Voronoi Tessellation Structure (VTS), which is then reduced to the Wigner-Seitz (WS) cell [45], or the primitive cell for all intents and purposes; this primitive cell is the mechanism of standardization that Magpie excels at in creating the crystal and composition features. Thus, no matter the initial crystal configuration that is available for a specific structure, especially the ones obtained in bulk from material databases' APIs, they can be reduced to their WS cell that is indeed smaller as well as more consistent, leading to a more accurate modeling process. More interestingly, this methodology can even be extended further to the unrelaxed crystal structures to generate the so-called "unrelaxed features" which can be used for prediction of virtual structures, namely, prototypes which will be covered later in this work, with the same results in comparison to relaxed features for many compounds. As the compound's unrelaxed crystal structure becomes closer to its relaxed peer, the prediction results become more accurate [38].

This aforementioned feature generation process resulted in 271 features that are created using the default properties in Magpie, 145 of those features relate to the composition of the material (based on properties presented in Table S1) and the rest correspond to the crystal configuration, which were then further processed to remove constant and quasiconstant features depending on their variance values. Additionally, Pearson and Spearman correlations were used in order to remove linearly and monotonically correlated features as well with thresholds of 0.8 for both, respectively, resulting in a refined 63 features that can offer a better generalized performance of the model, low computational cost, and a reduced model complexity to avoid overfitting problems that may arise. The final features are listed in Table S2.

2.4. Training and Building the Predictive ML Model. To build the predictive model for the total phonon band center, we have employed a general preliminary prediction process of the most commonly utilized algorithms in the field of material informatics and property predictive modeling (random forest [46, 47], decision trees [48, 49], AdaBoost [50], etc.). From this process, the most promising candidate algorithms to use for our dataset have been selected, and these are the extra regression trees (XT), gradient boosting (GB), extreme gradient boosting (XGB), and decision trees (DT). Expectedly, most of the promising algorithms belong to the ensemble family of learners, which are popularly used for regression modeling in this field [24]. Those algorithms have been used separately to create models on the initial dataset and have been involved in a 10-fold cross-validation process (10-fold CV) [51] to differentiate and subsequently select the working model for the next prediction phases. The performance of the various models built was examined using conventional regression error metrics, such as the R^2 metric, the mean absolute error (MAE), and the root mean squared error (RMSE) [52].

3. Results and Discussions

The 10-fold CV scores of the models built based on the 4 algorithms, as presented in Figure 2(a), show that the performance of XT-model is better than that of other models, where the R [2], RMSE, and MAE of this model were 0.964, 14.8 meV, and 7.9 meV, respectively, which are higher than the scores of the other models. The performance of the built models was also shown through a representative split

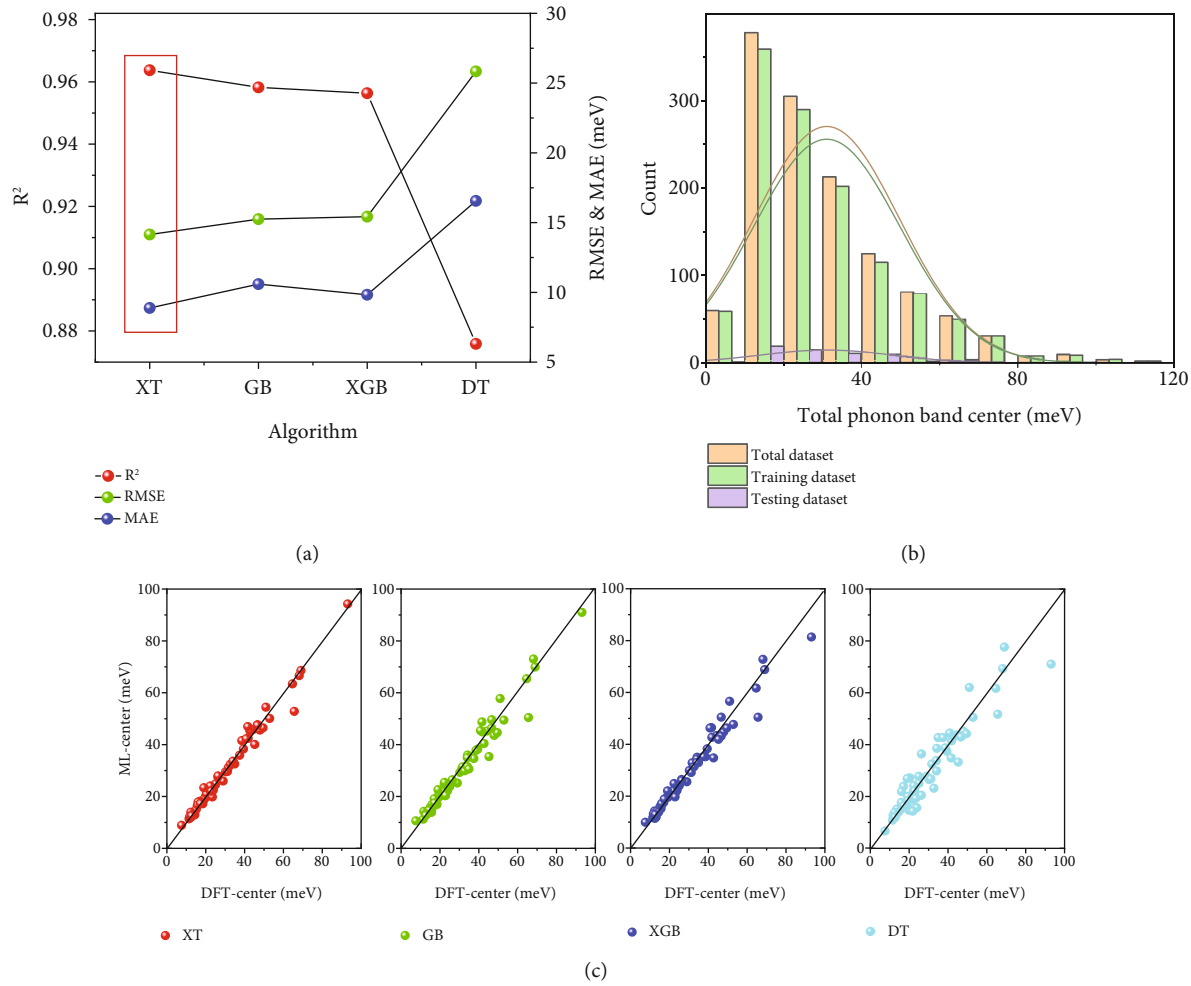

Figure 2: (a) Cross-validation results of the models (extra random trees (XT), gradient boosting (GB), extreme gradient boosting (XGB), and decision trees (DT)) built in the present work using 3 metrics including R [2], mean absolute error (MAE), and root mean squared error (RMSE). The XT-model was found to perform better than the other models. (b) A representative split (training set and testing set) that was used to visualize the testing results from the 4 models. (c) The testing results of the 4 built models conducted on the representative split, confirming that the XT-model is the most reliable among other models.

(Figure 2(b)), and here, the R^2 scores (XT: 0.964, GB: 0.957, XGB: 0.954, and DT: 0.871) obtained for the models based on this split were consistent with the cross-validation results in Figure 2(a). According to the cross-validation results and scores from the representative split presented in Figures 2(a) and 2(c), respectively, one can clearly suggest that the XT-model can be used as the primary model for further investigation in this work to explore solid electrolytes with high performance for Li-ion batteries. A particular note has to be underlined here, as the process of hyperparameter optimization has been ruled out from this work, and this is due to the fact that this optimization process is resource intensive which requires a fine grid of hyperparameters to cover a wide range and a suitable hyperparameter optimization (searching) algorithm that enables a fast yet reliable exploration and, consequently, fast computing power to sift through the model initialization process for each hyperparameter. This process has not been considered in this work, due to the promising performance of the XT-model with its original preset hyperparameters, as presented in Figures 2(a) and 2(c). Thus, a short discussion about the choice of hyperparameters is given in the supplementary materials and Table S3, and an insight into the feature's importance is given in Figure S2.

The results reached here regarding the performance of the XT-model can be supported additionally through an in-house validation process using DFT calculations conducted on new compounds, which were not included in the present learning process. For this purpose, 5 different compounds ($LiYO_3$, Li_2CO_4, $LiNiO_3$, $LiGeO_3$, and $LiSiO_3$) were selected for the validation process by DFT. Prior to this process, however, and to ensure that the quality and procedure of DFT PhDOS calculations are valid, the parameters to be used for the DFT calculations were adjusted though comparing the PhDOS results obtained in the present work with those of the same compounds from other sources. Specifically, the PhDOS calculations for the two compounds Li_3PO_4 and $LiAgF_6$ which were conducted by Muy et al.

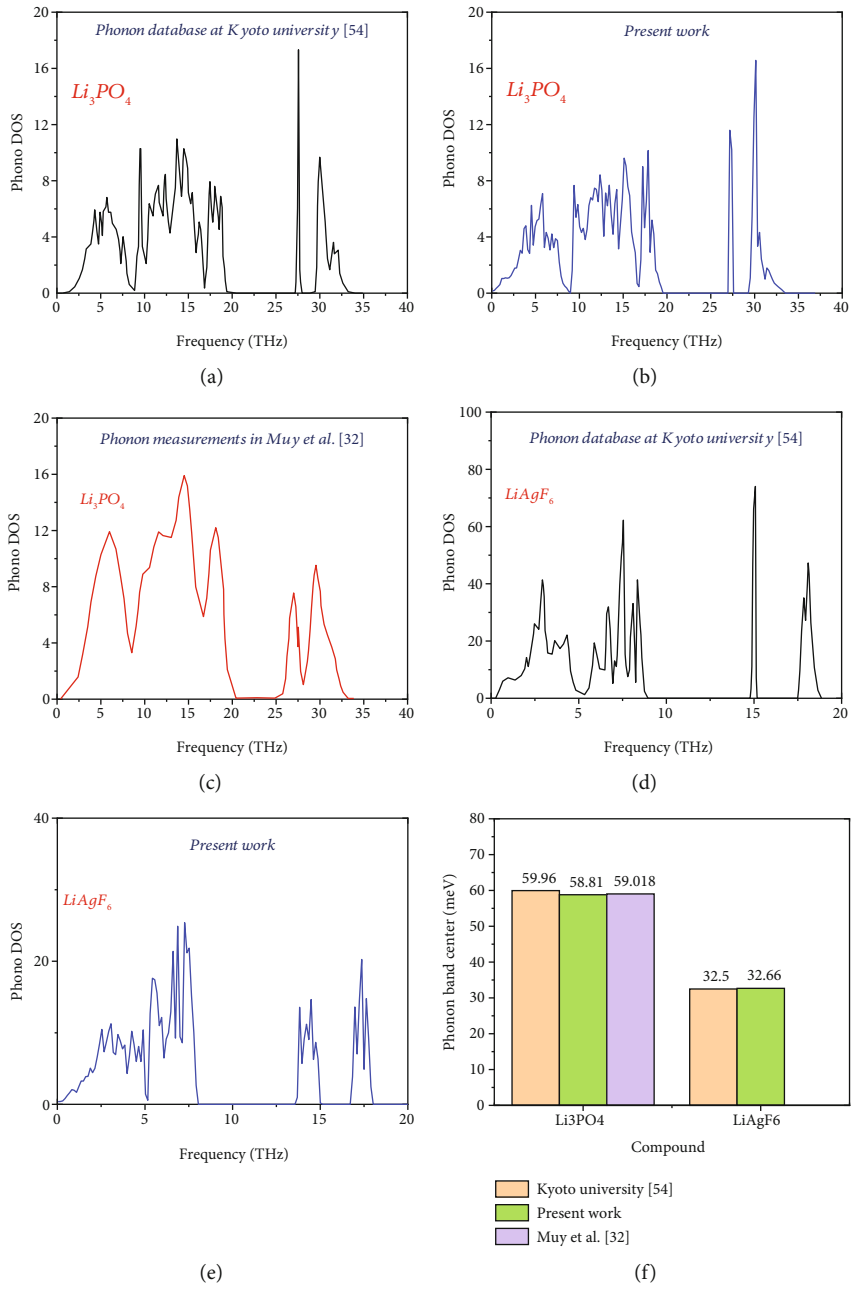

FIGURE 3: (a–c) PhDOS of the Li_3PO_4 (*Pnma*), as obtained from the Phonon Database at Kyoto University [53], calculated in the present work based on DFT, and experimentally measured using the wide-angular range chopper spectrometer (ARCS), as reported by Muy et al. [31]. (d, e) PhDOS of $LiAgF_6$ ($Ia\bar{3}$), as obtained from Phonon Database at Kyoto University [53] and as calculated in the present work based on DFT. (f) A comparison of the total phonon band centers determined for Li_3PO_4 and $LiAgF_6$ from their corresponding PhDOS presented in (a)–(e).

[31] and Togo and Tanaka [53], respectively, were used to provide a baseline of comparison for the in-house DFT calculations. The idea here is to ensure that our calculations are valid within the acceptable range of accuracy in comparison to other established reported works [31, 53] prior to the process of calculating PhDOS for new or unseen compounds from the promising ML-predicted pool.

The results obtained in the present work and those reported in other works are presented in Figures 3(a)–3(e). It is clearly seen from Figures 3(a)–3(c) that the PhDOS of Li_3PO_4 determined by the present DFT calculations were fairly in agreement with those calculated in the other works [31, 53], and this was also reached for $LiAgF_6$ (Figures 3(d) and 3(e)). More importantly, the consistency between the present results and the previous reported results was additionally confirmed through the total phonon band centers of the two compounds, which is the main focus here, as determined from the PhDOS calculations in Figures 3(a)–3(e) by Eq. (1), where the values of the total phonon band centers determined for each compound were very similar

with those determined in other works (Figure 3(f)). These results offer two important observations; first is that the DFT methodology employed here is fairly reliable and can be used for other compounds in order to validate the accuracy and viability of the XT-model built in this work. Secondly, the extremely small error between the DFT-calculated total phonon band center and the ones calculated from other sources for Li_3PO_4 (error: 1.15%) and $LiAgF_6$ (error: 0.49%) suggests that as long as there is a general overlap between the trend of the PhDOS obtained from the DFT calculations and experimental results obtained from any source pertaining to a specific material, i.e., the maximum and minimum frequencies, the location of the peaks and troughs, etc., the total phonon band center value is stable to noise and artifacts that result from the variation of DFT parameters (Figure S3 and S4), making the total phonon band center a powerful descriptive and predictive proxy in this case specifically. Additionally, some observations regarding PhDOS that is obtained from the previous sources has to be highlighted here; namely, the fact that the PhDOS data obtained from the Kyoto Univ. database [53] are mere preliminary calculations that give rudimentary information about the phonon dynamics and are not conclusive in their outcomes, which also suggests that a complete overlap of the PhDOS plots is quite difficult to achieve as is the case in $LiAgF_6$ that has been observed and negative frequencies could also suggest that the methodology of the calculation is flawed which is a considerable topic in off itself. That being the case, it is important to note that our approach to calculating the PhDOS relies heavily on establishing a fairly accurate methodology that can also be applicable at a rapid pace for new materials that have no calculations beforehand, which could provide some limitations to an in-depth analysis of the individual materials at hand. Yet, it is also considerable, here, to signify the importance of the total phonon band center proxy as it provides an overall weighted average singular value that can be interpreted within the context of ionic conductivity, given that the degree of accuracy is acceptable for the PhDOS calculations as have been pointed out earlier. Accordingly, DFT will be used to calculate the PhDOS of the 5 compounds, as indicated before ($LiYO_3$, Li_2CO_4, $LiNiO_3$, $LiGeO_3$, and $LiSiO_3$). The calculation results of the 5 compounds are presented in Figure 4(a) by the side of their crystal structure and space groups (Figure 4(b)). Total phonon band centers of these and those of some other Li-containing compounds (84 compounds) obtained from MP [34] that were not included in the initial dataset were determined using the PhDOS Eq. (1), and they were compared with the counterpart values predicted by the XT-model (Figure 4(c)). The results in Figure 4(c) prove the reliability of the built XT-model for predicting the total phonon band center, where R^2 of this validation process was 0.97, which is even higher than the value obtained in the cross-validation process (Figure 2(a)). Interestingly, the total phonon band center predicted by the XT-model for $LiSiO_3$, $LiGeO_3$, and $LiNiO_3$ exhibits a reasonable linearity with the unit cell volume of the counterpart compounds, as shown in Figure 4(d). As has been discussed before on LGPX [21], the ionic conductivity is directly affected by the volume of the unit cell within one family of electrolytes. Here, the 3 compounds ($LiXO_3$: X=Si, Ge, Ni) possess identical crystal characteristics, where they have a cubic structure, in which LiO_{12} cuboctahedra share corners with other 12 equivalent LiO_{12} cuboctahedra, faces with 6 equivalent LiO_{12} cuboctahedra, and faces with 8 equivalent XO_6 octahedra. In addition, one XO_6 octahedra shares the corners with 6 equivalent XO_6 octahedra and faces with 8 equivalent LiO_{12} cuboctahedra. Thus, considering the unit cell volume as a descriptor for ionic conductivity, one can simply arrange the ionic conductivity of the 3 compounds from low to high as follows, $LiSiO_3$, $LiGeO_3$, and $LiNiO_3$, and this sequence complements the predicted values obtained by the XT-model for total phonon band center. On one side, this finding additionally confirms the reliability of the built model, and from another, it further supports the suggestion that total phonon band center can be employed as an effective and practical ionic conductivity descriptor in the discovery process of high-performance solid electrolytes for Li-ion batteries.

Up to here, this model can be used to discover solid electrolytes with high ionic conductivity based on the total phonon band center. For this purpose, the features of ~17 K Li compounds presented in the MP database, which have no PhDOS calculations (methodology for obtaining those materials is presented in the supplementary materials), were generated and then used as inputs in the built XT-model to predict the total phonon band centers of each in the list. The ML-predicted values are shown in Figure 4(e) alongside the corresponding stability value of each compound. Nonstable compounds with stability values higher than 50 meV/atom were excluded, and those with values less than 50 meV/atom were highlighted, as shown in Figure 4(f). In general, the thermodynamic stability is evaluated using the concept of energy above convex hull (E_h) or convex hull distance, and here, the threshold of 50 meV/atom was selected due to the fact that this energy is calculated at 0 K based on DFT calculations, and accordingly, an additional value related to real conditions used in experiments is to be considered to alter this from its 0 meV/atom value [39]. The data presented in Figure 4(f) are arranged based on the expected feasibility of the compounds as ionic conductors, and that is following the total phonon band center value of these compounds, as predicted by the model in the present work. Per the tendency in Figure 4(f), the compounds related to the red-labeled region were separated (listed in supplementary materials) and a sample of those are listed in Table 1 (50 compounds) where those are predicted to exhibit a promising performance as Li-ion conductors. For experimental validation of the XT-model built in this work, two different compounds were selected from the low and high ranges of the total phonon band centers based on the threshold of 40 meV [31], and direct measurements of their ionic conductivities were conducted using electrochemical impedance spectroscopy (EIS). The first compound, Li_6PS_5Cl ($F\bar{4}3m$) with a total phonon band center of 33 meV, as predicted by the XT-model, is a well-known electrolyte with high ionic conductivity at RT [54]. On the other

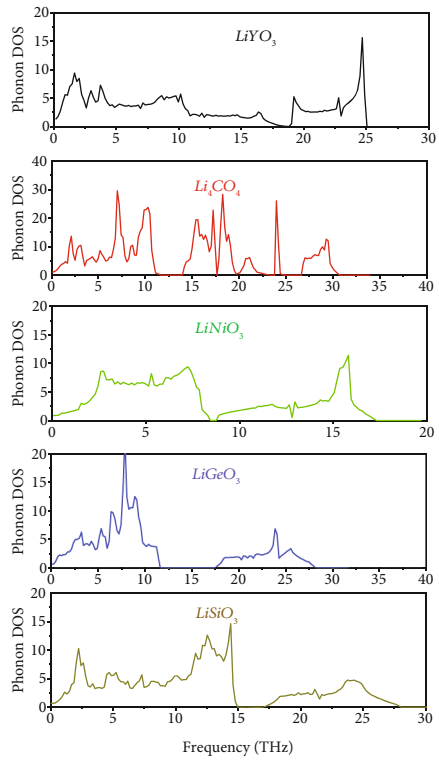

(a)

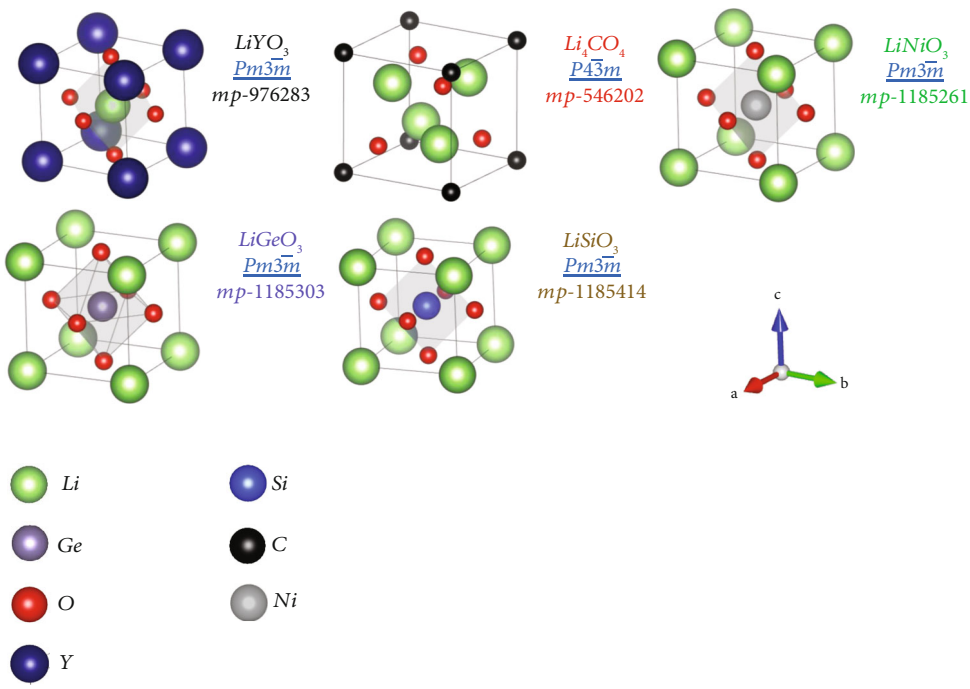

(b)

Figure 4: Continued.

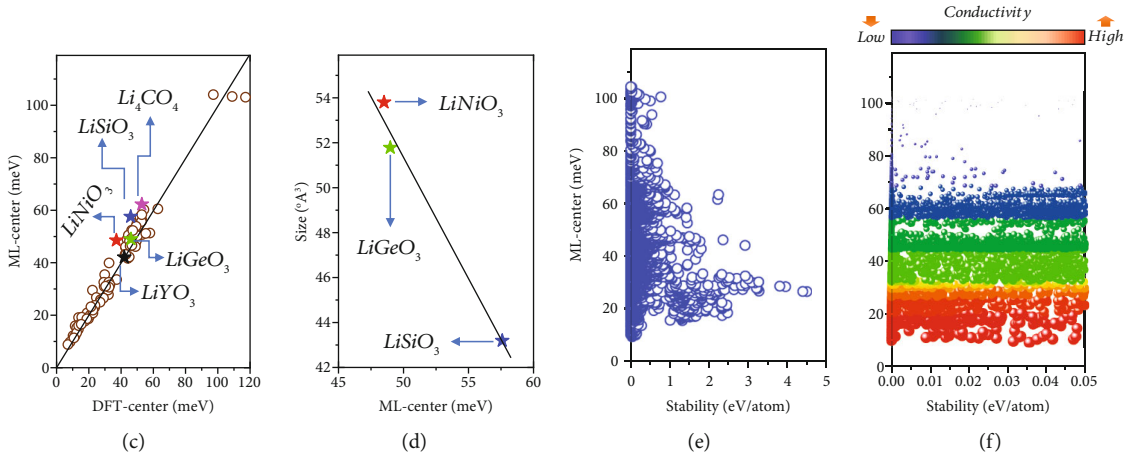

Figure 4: (a, b) PhDOS of $LiYO_3$ ($Pm\bar{3}m$), Li_4CO_4 ($P\bar{4}3m$), $LiNiO_3$ ($Pm\bar{3}m$), $LiGeO_3$ ($Pm\bar{3}m$), and $LiSiO_3$ ($Pm\bar{3}m$), as calculated in the present work using DFT, and their structures, respectively. (c) A comparison of the total phonon band centers calculated from (a) with those predicted by the XT-model built in the present work. This comparison was expanded to cover 84 Li-containing compounds that have PhDOS calculations, and those were obtained from Materials Project database but not included in the initial dataset. Good matching between the ML-predicted total phonon band centers (ML-center) and the DFT-calculated ones (DFT-center) with $R^2 = 0.970$. (d) The total phonon band centers predicted by the XT-model for the $LiNiO_3$ ($Pm\bar{3}m$), $LiGeO_3$ ($Pm\bar{3}m$), and $LiSiO_3$ ($Pm\bar{3}m$) as a function of the volume of the unit cell, supporting the hypothesis that the total phonon band center is a suitable proxy to represent ionic conductivity in the learning processes used in this work. (e) The total phonon band centers of ~17 K Li-containing compounds taken from MP, as predicted by the XT-model built in the present work. These compounds had no experimental or computational calculations related to the PhDOS beforehand. (f) The ML-predicted total phonon band centers of the compounds that are thermodynamically stable (<50 meV/atom). The red data points are expected to show high ionic conductivity according to their total phonon band centers, and this was additionally illustrated by the gradient color bar included in the figure.

hand, the second compound selected from the high range (>40 meV) is Li_2CO_3 ($C2/c$), which, in turn, has never been explored before for this kind of application. Before these experiments, the results of the ML prediction conducted on the two compounds were confirmed through the related DFT calculations. Figures 5(a)–5(c) show the PhDOS, structure, and estimated total phonon band center of the two compounds, respectively. The results showed that the values of the total phonon band center obtained through the ML predictions and estimated based on the DFT calculations are in agreement with relative errors of 6.04% for Li_6PS_5Cl and 0.45% for Li_2CO_3. The error for Li_6PS_5Cl in particular is quite considerable given the overall value of the total phonon band center, this error can be contributed to various reasons, and some of those can be discussed here; firstly, this material is in fact a complex compound in its composition and crystal configuration, which could add unwanted challenges in its DFT calculations such as optimal crystal size initiation and DFT parameter limitations which could impact the calculation process yet increase the computational time drastically. The other reason could be due to the fact that the XT-model simply requires more diversified training data to encapsulate the general behavior of Li_6PS_5X materials overall, which could be resolved if more data is added manually, which hinders the pace and requires extra attention to specific trends of materials in this field of study. Nevertheless, although the current error margins can definitely be improved by extensive analysis of the material at hand (Li_6PS_5Cl), the general trend of the behavior of the total phonon ban center can definitely be noted. Figure 5(d) shows the Nyquist plot of Li_6PS_5Cl conducted at various temperatures. Based on these measurements, the ionic conductivity (σ) of Li_6PS_5Cl at the various temperatures was determined using the following equation [55]:

$$\sigma = \frac{l}{A \bullet R}, \tag{3}$$

where l is the thickness of the Li_6PS_5Cl pellet used in the EIS measurements, A is the area in contact with the stainless-steel electrode of the spectroscope, and R is the ionic resistance of Li_6PS_5Cl, as determined by the spectroscopy profiles in Figure 5(d). This measurement shows that Li_6PS_5Cl exhibits high RT ionic conductivity (0.00291 S/cm) and low activation energy (~0.195 eV), as presented by Arrhenius plot inserted in Figure 5(d), and this is consistent with the findings obtained by the XT-model built in the present work, where Li_6PS_5Cl was predicted to have a low total phonon band center (32.3 meV). Regarding the high conductivity achieved by this compound, it is unsurprising given previous reports of its high ionic conductivity [54, 56, 57], which was attributed to the low activation energy associated with Li-ion conductivity. However, the noteworthy discovery here is the capability of the current XT-model to identify this compound without the requirement for elaborate experimental procedures. The EIS profiles of the second compound (Li_2CO_3) selected from the high range of the total phonon band center (Figure 4(f)) are presented in Figure 5(e). These profiles were recorded at various temperatures between RT and 180°C. It is clearly seen from Figure 5(e) that the profile terminated before intercepting the real axis, even at high temperatures (140 and 180°C), indicating a very high

Table 1: A sample list consisting of 50 promising Li compounds with low total phonon band center (<40 meV) out of ~17 K Li compounds that have been used for prediction. Additional information regarding the stability, chemical system, crystal system, and space group is shown as well.

System	mp-id	Composition	Predicted center (meV)	Stability (eV/atom)	Crystal system	Space group
Li-S	mp-756086	Li_5BiS_4	22.65097241	0.0957989225	Orthorhombic	$Pmmn$
	mp-766467	LiCuS	23.1757682	0.04040561625	Orthorhombic	$Pbcn$
	mp-1153	Li_2S	27.2939112	0	Cubic	$Fm\bar{3}m$
	mp-8430	KLiS	34.74791424	0	Tetragonal	$P4/nmm$
	mp-30248	$LiMoS_2$	35.81351741	0.02264577313	Triclinic	$P\bar{1}$
	mp-1001786	$LiScS_2$	36.59939717	0	Trigonal	$R\bar{3}m$
	mp-1195718	$Li4SnS_4$	36.88014076	0	Orthorhombic	$Pnma$
	mp-867699	$Li4TiS_4$	38.02538759	0.009325313333	Tetragonal	$I\bar{4}2m$
	mp-30249	$Li4GeS_4$	32.54642619	0	Orthorhombic	$Pnma$
	mp-1188392	$LiInS_2$	33.75133085	0	Orthorhombic	$Pna2_1$
	mp-767516	Li_9Sb_3S	29.83087585	0.08155559199	Monoclinic	$P2_1/c$
	mp-755470	Li_2BiS_2	26.08057	0.097352	Orthorhombic	$Imm2$
	mp-755470	Li_2BiS_2	26.08057	0.097352	Orthorhombic	$Imm2$
	mp-696123	$Li_{10}Sn(PS_6)_2$	27.61404768	0.0333131094	Tetragonal	$P4_2mc$
Li-Se	mp-2286	Li_2Se	24.83585183	0	Cubic	$Fm\bar{3}m$
	mp-30100	$Li_2B_2Se_5$	27.25385145	0	Monoclinic	$C2/c$
	mp-10231	$LiMnSe_2$	34.99314872	0.09420128891	Trigonal	$P3m1$
	mp-28603	NaLiSe	35.78187931	0	Orthorhombic	$Pnma$
	mp-1095291	Li_2SnSe_3	36.62822339	0	Monoclinic	Cc
	mp-1211446	Li_7PSe_6	36.94008782	0	Orthorhombic	$Pna2_1$
	mp-9250	RbLiSe	38.02751925	0	Tetragonal	$P4/nmm$
	mp-10618	$LiInSe_2$	32.6480686	0.0813290375	Trigonal	$R\bar{3}m$
	mp-15794	$LiYSe_2$	37.11410118	0	Trigonal	$R\bar{3}m$
	mp-973793	Li_8SeN_2	36.42267101	0	Tetragonal	$I4_1md$
Li-O	mp-28592	$Li_7Br_3O_2$	23.60890704	0.02552174042	Tetragonal	$I4/mmm$
	mp-778878	$BaLi_4O_3$	25.08419013	0.08632171469	Orthorhombic	$Cmc2_1$
	mp-8412	$LiCeO_2$	26.46322331	0.03886750766	Monoclinic	$P2_1/c$
	mp-29077	$LiBiO_3$	27.79402223	0	Orthorhombic	$Pccn$
	mp-1306939	Li_2CrO_3	29.84134526	0.044340775	Monoclinic	$C2$
	mp-1173952	$Li_3Mn_2O_5$	33.31552984	0.0227905305	Monoclinic	$C2/m$
	mp-1211142	Li_5IO_6	33.78752157	0	Trigonal	$P3_112$
	mp-691115	Li_4Mn5O_{12}	34.41020385	0	Monoclinic	$C2/c$
	mp-14495	Li_6ZnO_4	37.09048767	0	Tetragonal	$P4_2/nmc$
	mp-756664	$LiFeBO_3$	39.64993618	0.005343331111	Hexagonal	$P\bar{6}$
Li-Se-O	mp-1198324	$Li_2B_8SeO_{15}$	39.32083332	0	Monoclinic	$P2_1/c$
	mp-770832	Li_2BSeO_4	39.95422648	0.05752937621	Monoclinic	$P2_1/c$
	mp-1198324	$Li_2B_8SeO_{15}$	39.32083332	0	Monoclinic	$P2_1/c$
Li-S-O	mp-1020018	$Li_5B(SO_4)_4$	39.18512326	0.00091758125	Monoclinic	$P2_1/c$
	mp-1020060	$LiB(S_2O_7)_2$	39.18689863	0	Orthorhombic	$P2_12_12_1$
	mp-1020106	$LiB(SO_4)_2$	39.19494269	0	Monoclinic	Pc
	mp-1105750	$LiAu(S_2O_7)_2$	38.23145519	0	Triclinic	$P\bar{1}$

Table 1: Continued.

System	mp-id	Composition	Predicted center (meV)	Stability (eV/atom)	Crystal system	Space group
	mp-768754	$LiBi_2(SO_4)_3$	41.126971	0.09646661291	Monoclinic	$P2_1/c$
	mp-765354	$Li_2Co_2(SO_4)_3$	45.13286191	0.03155810283	Orthorhombic	*Pbca*
	mp-1176804	$LiCo(SO_4)_2$	45.05950178	0.07157163193	Triclinic	*P*1
	mp-774921	$KLiNiO_2$	38.36338	0.057834	Monoclinic	*C*2/*m*
	mp-753282	Li_2MnOF_3	34.96503	0.033177	Monoclinic	*C*2/*m*
	mp-15551	Sr_2LiSi_3	26.47019383	0	Orthorhombic	*Fddd*
	mp-982974	$LiBeAu_2$	31.21852323	0.002375858125	Cubic	$Fm\bar{3}m$
Other	mp-29025	Li_5Br_2N	35.82069002	0.003017267559	Orthorhombic	*Immm*
	mp-1663705	$Li_7Ni(O_2F)_2$	38.07896974	0.09718476679	Triclinic	*P*1
	mp-573471	$Li_{17}Sn_4$	29.18006	0	Cubic	$F\bar{4}3m$

resistance and poor ionic conductivity of Li_2CO_3. The low ionic conductivity is mainly attributed to the high enthalpy of Li-ion migration within this compound, as has been found through DFT calculations conducted in the present work. The calculations of migration enthalpies for Li_2CO_3 presented in Figure 5(f) showed that the energy barrier needed for a Li ion to migrate from one lattice position to the next is equal to 0.998 ± 0.05 eV, which is higher than that determined for Li_3PO_4 (0.723 eV, Figure 5(g)).

After narrowing down our focus to the compounds predicted to show a total phonon band center that is below 40 meV, serving as a threshold for promising electrolytes, we observed that Li-S, Li-O, and Li-Se chemical systems exhibit the lowest total phonon band center of the bunch. Some of them are presented Figure 6(a) and are classified according to their anions into oxides, sulfides, and selenides. Interestingly, the values of the total phonon band center of the three families, as predicted by the XT-model in Figure 6(a), are consistent with the general trend of the conductivity in oxide and sulfide families as well as the relative feature importance (Gini Importance) that have been obtained from the XT-model (Figure S2), and those important features, mainly "min_CovalentRadius" and "min_GSvolume_pa" which represent the minimum covalent radius as well as the ground state volume of the unit cell of the materials, corroborate the well-established correlation between the ionic conductivity and the crystal size, evidenced by the ionic conductivity of sulfide-based electrolytes which is higher than that of the counterpart oxide-based electrolytes, such as Li_3PS_4 and Li_3PO_4, that is contributed to the crystal size effect [31]. This factor can be applicable when we compare the selenide-based electrolytes with the sulfide-based electrolytes, suggesting that selenide-based ones have a greater potential to be used as solid electrolytes in LIBs, where they show lower values of total phonon band center as compared to those in the two other families (oxides and sulfides). In this context, despite not having any prior background or knowledge in physical and chemical notions, the model acquired the ability to learn and use such knowledge, enabling it to predict trends that align closely with actual observations. This list shown in Figure 6(a) (given in supplementary materials) is an initial step, which offers researchers a guided foundation to advance their efforts in the fabrication and characterization of high-performance electrolytes for LIBs. From this list and as a promising electrolyte, $LiBiO_2$ (*Ibam*) was selected for further investigations. DFT-based PhDOS and migration enthalpy calculations were conducted for this compound. The PhDOS results of $LiBiO_2$ alongside its structure are presented in Figures 6(b)–6(d). The total phonon band centers estimated from Figure 6(b) using Eq. (1) for this compound exhibit excellent agreement with the value predicted by the XT-model, showing a relative error percentage of 3.46%. The migration enthalpy calculations presented in Figure 6(e) further confirm the findings reached by the learning process, where the energy barrier for Li-ion migration in $LiBO_2$ was found to be less than that of Li_2CO_3 (0.998 vs. 0.271 ± 0.05 eV, Figures 6(e) and 5(f), respectively). Surprisingly, the value obtained was even lower than that recorded for Li_3PS_4 (0.296 eV) [31] (Figures 6(f) and 6(g)), which is a recognized high-performance electrolyte employed in solid-state LIBs with barriers close to those of liquid electrolytes used in traditional LIBs. This result is quite interesting since oxide-based electrolytes are easier to prepare as compared to sulfide-based, where contamination with oxygen is a critical issue during the preparation of these electrolytes (sulfide-based) [58, 59]. Accordingly, through the present learning process, an oxide-based electrolyte was predicted to exhibit an improved performance, which can be comparable to conventional liquid and solid electrolytes.

Up to here, we have reached a point where the present work must give some other useful directions for further investigations and experimental works on the fabrication and characterization of superconductors for LIBs. This can be carried out through considering the main potential of the employed features (Magpie), which is useful for describing compounds constructed from scratch, with no information about their relaxed structures. This can be done starting from well-known electrolytes, such as NASICON- or LISICON-structured solid electrolytes, and by a chemical

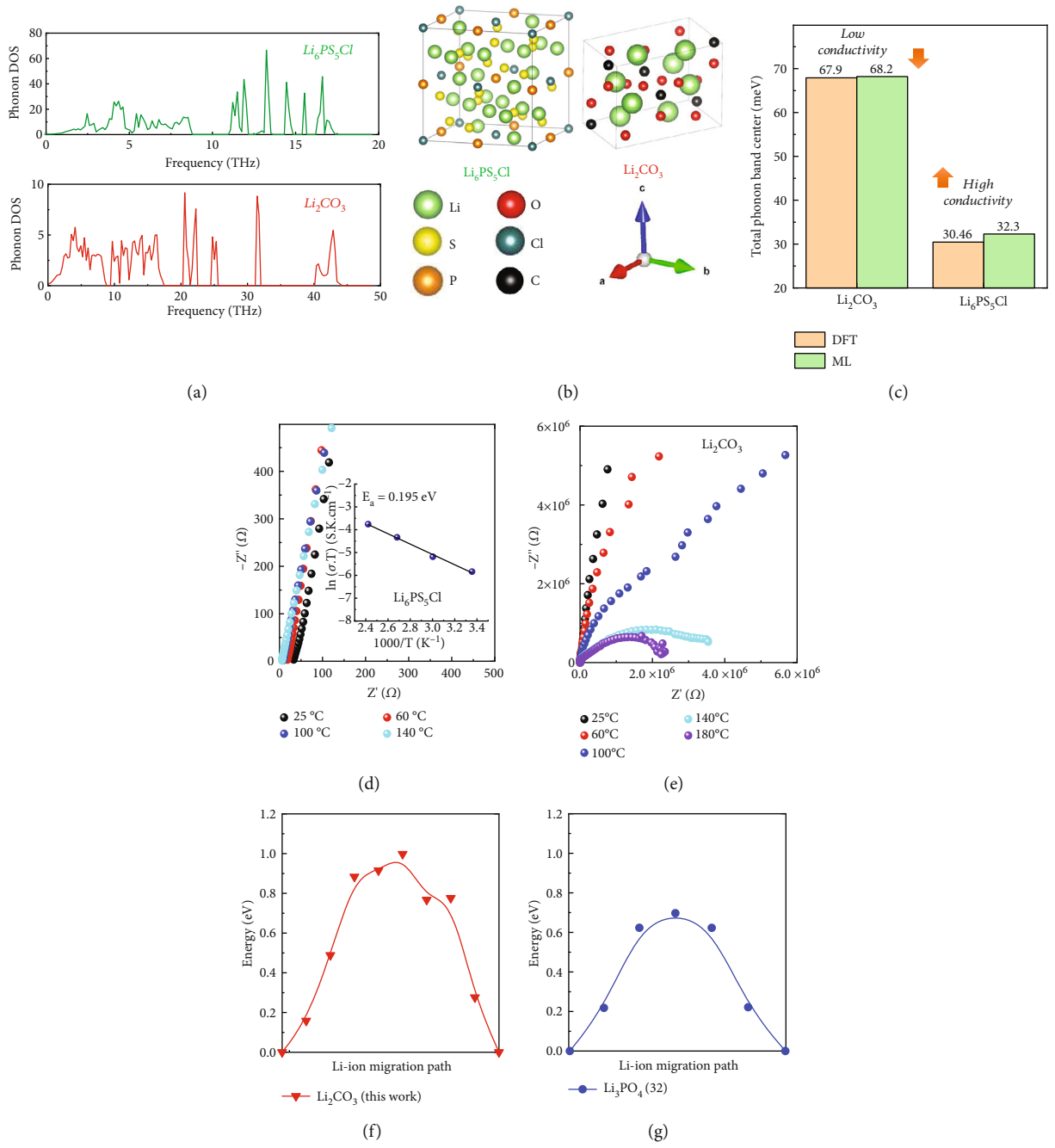

FIGURE 5: (a, b) PhDOS of Li_6PS_5Cl ($F\bar{4}3m$) and Li_2CO_3 ($C2/c$), as calculated in the present work using DFT, and their structures, respectively. (c) A comparison of the total phonon band centers calculated from (a) with those predicted by the XT-model built in the present work for Li_6PS_5Cl and Li_2CO_3. The relative error between the DFT-calculated and ML-predicted values for Li_6PS_5Cl and Li_2CO_3 are presented in (c). (d, e) EIS profiles for Li_6PS_5Cl and Li_2CO_3 recorded at various temperatures. The figure inserted in (d) presents the Arrhenius plot of Li_6PS_5Cl, as constructed from the ionic conductivities determined at the various temperatures in (d), and by this plot, the activation energy was estimated to be 0.195 eV. (f, g) DFT calculations of the migration enthalpy of Li ions in Li_2CO_3 and Li_3PO_4 ($Pmn2_1$) [31], respectively.

substitution process, structures of numerous nonrelaxed compounds can be generated. One example of this process is given in Figure 7(a) for NASICON-structured electrolyte. Starting from $LiGe_2(PO_4)_3$ with ($R3c$) space group, a well-known solid electrolyte in LIBs, and by chemical substitution of Ge, P, and O with elements highlighted in the periodical table (Figure 7(a)), the structure of $LiC_2(C'X_4)_3$ nonrelaxed compounds was generated where C, C′, and X are the generic elements that can be substituted according to our scheme (the distinction between C and C′ and other details about this process are given in the supplementary materials, Figure S4 and Table S4). This procedure was also conducted

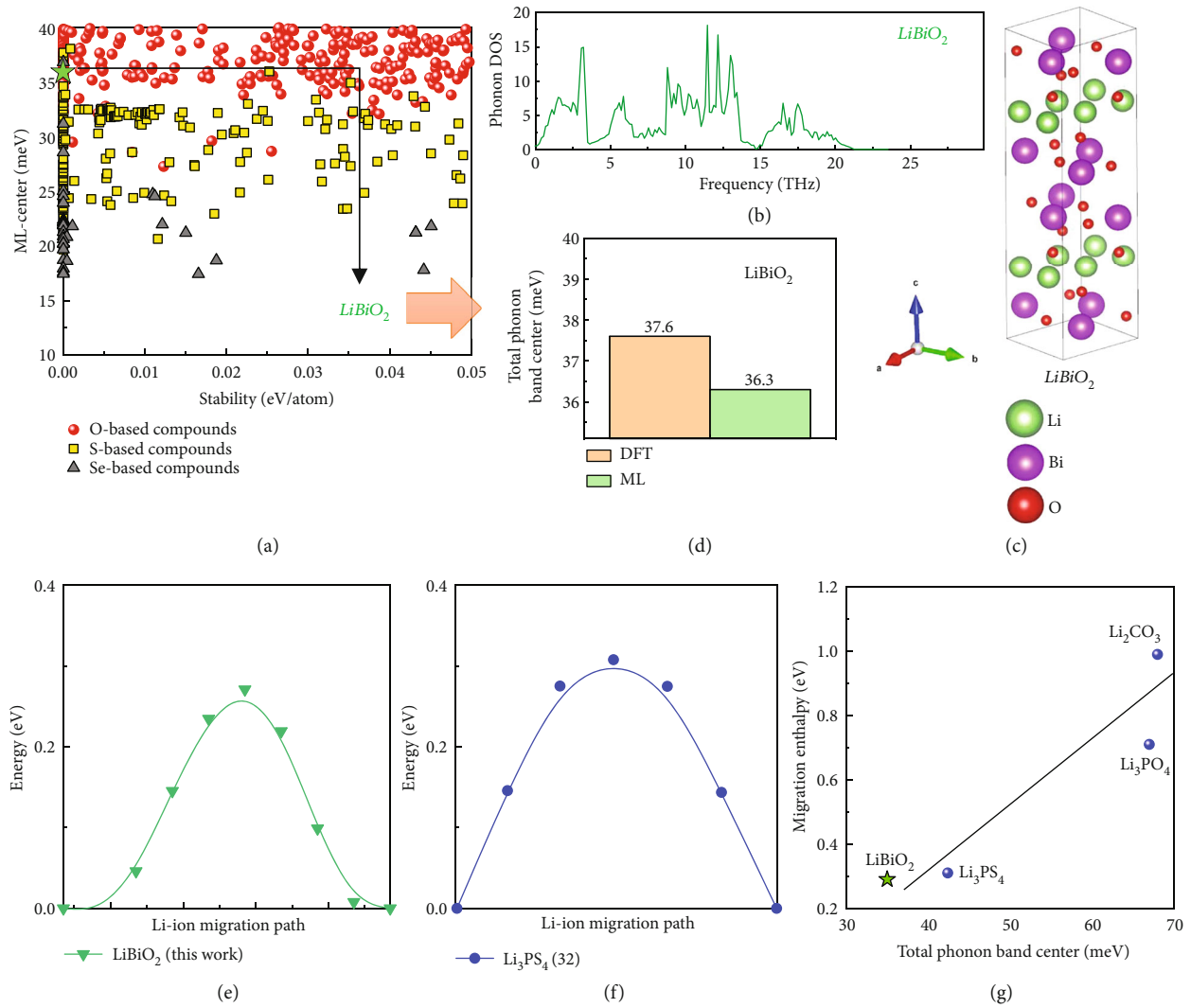

Figure 6: (a) The ML-predicted total phonon band centers of stable Li compounds ($E_h < 0.05$ eV/atom), which are expected to show high ionic conductivity. Those compounds were classified based on the chalcogen into O-based, S-based, and Se-based compounds. (b) PhDOS of $LiBiO_2$ (*Ibam*), as calculated in the present work using DFT. (c) The structure of $LiBiO_2$. (d) The total phonon band centers of $LiBiO_2$, as predicted by the XT-model, and the corresponding values determined by DFT calculations in the present work. A relative error of 3.46% was estimated between the ML-predicted and DFT-calculated values. (e) DFT calculations of the migration enthalpy of Li ions in the promising electrolyte ($LiBiO_2$), which was discovered by the XT-model. (f) DFT calculations of the migration enthalpy of Li ions in the traditional electrolytes, Li_3PS_4 (*Pnma*) [31]. $LiBiO_2$ demonstrates a lower migration enthalpy for Li ions compared to the Li_3PS_4 electrolyte (0.271 vs. 0.296 eV), which equates to a high ionic conductivity. This suggests that $LiBiO_2$ holds great potential as an electrolyte material for solid-state LIBs. (g) Migration enthalpy of Li ions as function to the total phonon band center of $LiBiO_2$, Li_3PS_4 [31], Li_3PO_4 [31], and Li_2CO_3.

on five notable solid electrolytes; those are Garnet type (LLZO), perovskite, argyrodites, LGPS, and LiPS where the chemical substitution for those prototypes followed the structure of the electrolyte. In total, the structure of 230,136 virtual compounds was constructed. The features of these compounds, as generated by the Magpie platform, were used as inputs in the XT-model built in the present work to predict the total phonon band center of the constructed compounds. Figure 7(b) shows the histogram of the total phonon band center predictions of the nonrelaxed structures obtained from the first prototype ($LiGe_2(PO_4)_3$). The histograms of other prototypes are presented in the supplementary materials (Figure S6), and a working sample of the most promising virtual compounds is given in Table S5. It can be observed from Figure 7(b) that 103,452 out of 179,395 NASICON-structured virtual compounds exhibit a predicted total phonon band center value less than 40 meV. For other prototypes (Garnet type (LLZO), perovskite, argyrodites, LGPS, and LiPS), 30,501 compounds were found to show low band centers (<40 meV) as well, suggesting that these virtual compounds can be used as part of a database from which promising solid electrolytes are screened for further investigations.

Figures 7(c)–7(h) show the predicted band centers of nonrelaxed structures as a function of the feature "mean_row," which is the mean value of the individual row

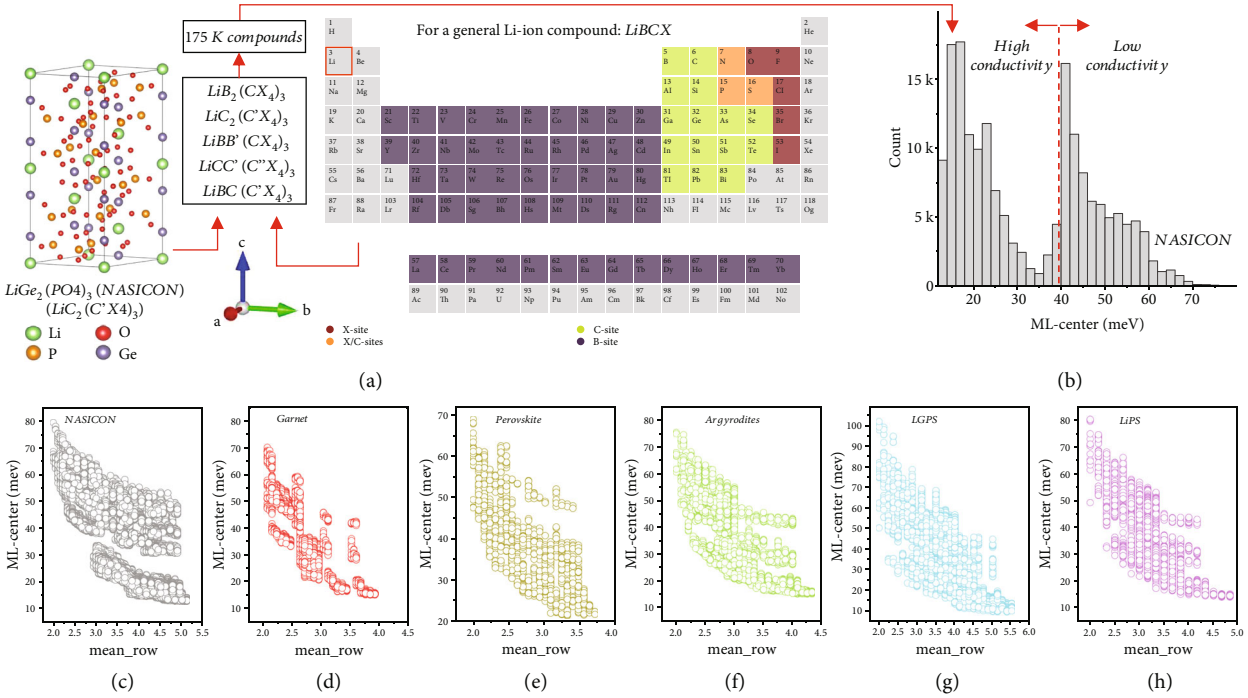

FIGURE 7: (a) The structure of $LiGe_2(PO_4)_3$ used as a prototype to generate new virtual compounds with nonrelaxed structures, for which the total phonon band center is to be predicted using the XT-model built in this work, and the related periodic table which is highlighted to the show the chemical substitution in this structure. The substitution procedures used for five other structures are introduced in the supplementary materials (Figures S5 and Table. S4). (b) Histogram of the total phonon band center, as predicted by the XT-model for the nonrelaxed structures constructed based on the NASICON-structured: $LiGe_2(PO_4)_3$ (*R3c*). Prediction of the other prototypes, including Garnet type (LLZO): $Li_7La_3Zr_2O_{12}$ (*I*41/*acd*), perovskite: Li_2TiO_3 (*C*2/*c*), argyrodites: Li_6PS_5Cl ($F\bar{4}3m$) LGPS: $Li_{10}GeP_2S_{12}$ (*P*1), and LiPS: Li_3PS_4(*Pnma*), is presented in the supplementary materials (Figure S6, Table S5). (c–h) The predicted values of the total phonon band center of the nonrelaxed structures constructed based on the various prototypes previously mentioned.

placement for each element in the composition according to their position in the periodic table. Interestingly, Figures 7(c)–7(h) show remarkable trends of decreasing total phonon band centers with increasing "mean_row" feature values, and this is in accordance with what we have discussed before on the effect of the crystal size on the ionic conductivity.

All in all, this work provides a new perspective on the predictive modeling of Li-ion solid electrolyte performance using an accessible and rapid proxy, total phonon band center, that allows for multiple applications in the field on Li-ion industry for reliable initial screening of promising Li-ion candidates prior to experimental investigations that could be laborious. Yet, the proposed framework of discovery is only a stepping stone in this field, and this framework could definitely be expanded by increasing the initial data pool and establishing a model that is based on experimental characterization of PhDOS rather than computational results. Additionally, the applicability of this model can be further expanded on the prediction of new solid-state Na-, Mg-, and Zn-ion electrolytes that have a superior performance in a field that is in dire need of new solid-state, cheap, and easily synthesized materials for battery applications. Thus, more works based on theoretical calculations and experimental investigations will be needed for further understanding of the composition-structure-property relationships in solid electrolytes for LIBs and the application of statistical modeling in this field in specific.

4. Conclusion

The present work was designed to build an ML model that can be used to discover high-performance ceramic electrolytes for solid-state LIBs. For this purpose, PhDOS calculations of ~1272 compounds (114 Li-containing compounds) were involved in a learning process, where the total phonon band center was used as a proxy to represent ionic conductivity in the learning process. The results showed that the model built based on extra random tree (XT) algorithm performs accurately with high scores as compared to other models employing different algorithms. This was also confirmed through an experimental validation process using electrochemical impedance spectroscopy (EIS) measurements conducted for Li_6PS_5Cl (high ionic conductivity) and Li_2CO_3 (low ionic conductivity). For discovering high-performance electrolytic materials, the built XT-model was involved in a large-scale prediction process conducted on relaxed structures, which included 17,114 Li compounds from the MP database, and this was conducted on 230,136 nonrelaxed structures obtained from 6 prototypes for well-known solid electrolytes in LIBs. In total, 136,041 compounds, from both relaxed and nonrelaxed, were predicted

to have low values of total phonon band center (<40 meV), suggesting that these materials have the potential to show high ionic conductivity. The migration enthalpy calculations of $LiBiO_2$, taken from the relaxed list with a predicted band center of ~36 meV, proved that this compound is a promising candidate as a Li-ion conductor, where it had a migration enthalpy of 0.27 ± 0.05 eV, which is comparable to that of the liquid-state electrolytes.

5. Methods

5.1. Experimental Analysis. The electrochemical impedance spectroscopy (EIS) experiments were conducted to determine the ionic conductivity of Li_2CO_3 and Li_6PS_5Cl at various temperatures. Li_2CO_3 and Li_6PS_5Cl were provided by Sigma-Aldrich. Pellets of the two materials (Li_2CO_3 and Li_6PS_5Cl) were prepared by cold-pressing the sample under a pressure of 60 MPa. The EIS measurements were performed with a Zive Lab MP2 (WonA-Tech, Korea) in the frequency range from 0.1 Hz to 100 kHz at the voltage amplitude of 5 mV.

5.2. First-Principle Calculations

5.2.1. Phonon Calculations. To calculate the PhDOS for the compounds (Li_3PO_4 and $LiAgF_6$), the Quantum ESPRESSO (QE) [60] platform was used to calculate the SCF calculations which is then used to generate the force sets using the Phonopy [61] extension that has been postprocessed further for the generation of the PhDOS data. First, we have pinpointed the space group of the compounds to be used and have generated a consistent $2 \times 2 \times 2$ primary supercell for the relaxed primitive cell of the initial structures. Those primary supercells have been involved in a PhDOS calculation procedure using Phonopy within the QE environment; initially, a finite displacement of 0.01 Å was given, according to the so-called small displacement method [62, 63] where the total energy and the effective potential are derived from finite-difference approximations for the supercell according to the Phonopy default preset and depending on the symmetry of the supercell as well. Next, those displacements create a list of modified supercells that are then calculated using the conventional ab initio methodology; thus, the calculations have been carried out using the Perdew–Burke–Ernzerhof (PBE) exchange correlation functional and the generalized gradient approximation (GGA) provided by the QE DFT package. The calculations of the energy and stress have been carried out consistently on the supercells of the specified compounds (Li_3PO_4 and $LiAgF_6$ and $LiYO_3$, Li_2CO_4, $LiNiO_3$, $LiGeO_3$, and $LiSiO_3$), and the calculations were done using a $5 \times 5 \times 5$ dense k-point mesh for the supercells and an optimized cutoff energy of ~50 eV for most of the compounds. A fine self-consistent convergence threshold of 10^{-6} eV for the energy calculations has also been utilized in order to avoid any divergence that would occur at lower thresholds. The choice of $5 \times 5 \times 5$ here is an optimized mesh according to the size of the specific input supercells after displacement and the accuracy calculations done on lower meshes; an increase in the k-point mesh above the $5 \times 5 \times 5$ threshold will indeed increase the accuracy slightly, yet it will lead to a significant increase in computational burden overall; thus, $5 \times 5 \times 5$ can indeed be used for the purposes of this study. Phonopy was then used to calculate the force constants to determine the local stresses in the supercell and determine the finite force differences. This force set is then used to generate the PhDOS using the densest Monkhorst-Pack sampling grid for each compound according to the available computational resources ($25 \times 25 \times 25$ grid on average), and due to the fact that the presence of PhDOS artifacts hardly influenced the value of the total phonon band center generally, an increase in the Monkhorst-Pack mesh does not vary the total phonon band center by a significant amount (Figure S3 and Figure S4).

5.2.2. Li-Ion Migration Energy Calculations. To calculate the migration energy of Li_2CO_3 and $LiBiO_2$, the climbing image nudged elastic band (NEB) methodology [64] as implemented in the Quantum ESPRESSO (QE) environment has been used. A $2 \times 2 \times 2$ supercell of Li_2CO_3 and $LiBiO_2$ has been used to initiate the initial and final states using void migration to relax the atomic positions only in both states and obtain an equivalent energy that indicates that both states are symmetrically equivalent. In the relaxation of both compounds, those calculations have been carried out consistently on the $2 \times 2 \times 2$ supercell of the two compounds that are to be used, with a $5 \times 5 \times 5$ dense k-point mesh and a preset default cutoff energy for both compounds as recommended by the QE platform according to the used pseudopotentials. A fine self-consistent convergence threshold of 10^{-6} eV for a smooth convergence for the energy calculations has also been utilized as previous phonon calculations. For the NEB calculations, 10 images to be calculated have been used in both compounds, the error threshold has been set to 0.005 eV/atom, and a climbing image scheme has been implemented similarly to both. Additionally, identical parameters have been used for the relaxation control of the NEB calculations as well.

Data Availability

The data is available upon request from the authors.

Conflicts of Interest

The authors declare that they have no conflicts of interest.

Acknowledgments

This work was supported by the Industrial Innovation Talent Growth Project of the Korean Ministry of Trade, Industry and Energy funded by Korea Institute for Advancement of Technology (#P0023676, Expert Program for Sustainable Metals Industry).

Supplementary Materials

The supplementary materials for this manuscript are attached in "Final_Supplementary Materials.docx" file. The supplementary file contains the necessary supplementary

information regarding data collection, feature engineering, DFT mesh, and prototypes. *(Supplementary Materials)*

References

[1] T. Kim, W. Song, D.-Y. Son, L. K. Ono, and Y. Qi, "Lithium-ion batteries: outlook on present, future, and hybridized technologies," *Journal of Materials Chemistry A*, vol. 7, no. 7, pp. 2942–2964, 2019.

[2] Y. Chen, Y. Kang, Y. Zhao et al., "A review of lithium-ion battery safety concerns: the issues, strategies, and testing standards," *Journal of Energy Chemistry*, vol. 59, pp. 83–99, 2021.

[3] J. W. Braithwaite, A. Gonzales, G. Nagasubramanian et al., "Corrosion of lithium-ion battery current collectors," *Journal of the Electrochemical Society*, vol. 146, no. 2, p. 448, 1999.

[4] D. Zhou, D. Shanmukaraj, A. Tkacheva, M. Armand, and G. Wang, "Polymer electrolytes for lithium-based batteries: advances and prospects," *Chem*, vol. 5, no. 9, pp. 2326–2352, 2019.

[5] J. Feng, L. Wang, Y. Chen, P. Wang, H. Zhang, and Z. He, "PEO based polymer-ceramic hybrid solid electrolytes: a review," *Nano Convergence*, vol. 8, 2021.

[6] G. S. Hegde and R. Sundara, "A flexible, ceramic-rich solid electrolyte for room-temperature sodium–sulfur batteries," *Chemical Communications*, vol. 58, no. 63, pp. 8794–8797, 2022.

[7] E. J. Cheng, T. Kimura, M. Shoji, H. Ueda, H. Munakata, and K. Kanamura, "Ceramic-based flexible sheet electrolyte for Li batteries," *ACS Applied Materials & Interfaces*, vol. 12, no. 9, pp. 10382–10388, 2020.

[8] K. Pan, L. Zhang, W. Qian et al., "A flexible ceramic/polymer hybrid solid electrolyte for solid-state lithium metal batteries," *Advanced Materials*, vol. 32, no. 17, article e2000399, 2020.

[9] T. K. Schwietert, V. A. Arszelewska, C. Wang et al., "Clarifying the relationship between redox activity and electrochemical stability in solid electrolytes," *Nature Materials*, vol. 19, no. 4, pp. 428–435, 2020.

[10] A. Guéguen, D. Streich, M. He et al., "Decomposition of LiPF 6 in high energy lithium-ion batteries studied with online electrochemical mass spectrometry," *Journal of the Electrochemical Society*, vol. 163, no. 6, pp. A1095–A1100, 2016.

[11] J. B. Goodenough, H. Y.-P. Hong, and J. A. Kafalas, "Fast Na +-ion transport in skeleton structures," *Materials Research Bulletin*, vol. 11, no. 2, pp. 203–220, 1976.

[12] M. Guin and F. Tietz, "Survey of the transport properties of sodium superionic conductor materials for use in sodium batteries," *Journal of Power Sources*, vol. 273, pp. 1056–1064, 2015.

[13] S. Roy and P. P. Kumar, "Influence of cationic ordering on ion transport in NASICONs: molecular dynamics study," *Solid State Ionics*, vol. 253, pp. 217–222, 2013.

[14] S. Song, J. Lu, F. Zheng, H. M. Duong, and L. Lu, "A facile strategy to achieve high conduction and excellent chemical stability of lithium solid electrolytes," *RSC Advances*, vol. 5, no. 9, pp. 6588–6594, 2015.

[15] B. Tao, C. Ren, H. Li et al., "Thio-/LISICON and LGPS-type solid electrolytes for all-solid-state lithium-ion batteries," *Advanced Functional Materials*, vol. 32, no. 34, article 2203551, 2022.

[16] C. Wang, K. Fu, S. P. Kammampata et al., "Garnet-type solid-state electrolytes: materials, interfaces, and batteries," *Chemical Reviews*, vol. 120, no. 10, pp. 4257–4300, 2020.

[17] S. Yan, C.-H. Yim, V. Pankov et al., "Perovskite solid-state electrolytes for lithium metal batteries," *Batteries*, vol. 7, 2021.

[18] Y. Lee, J. Jeong, H. J. Lee et al., "Lithium argyrodite sulfide electrolytes with high ionic conductivity and air stability for all-solid-state Li-ion batteries," *ACS Energy Letters*, vol. 7, no. 1, pp. 171–179, 2022.

[19] A. Kuhn, O. Gerbig, C. Zhu, F. Falkenberg, J. Maier, and B. V. Lotsch, "A new ultrafast superionic Li-conductor: ion dynamics in Li11Si2PS12 and comparison with other tetragonal LGPS-type electrolytes," *Physical Chemistry Chemical Physics*, vol. 16, no. 28, pp. 14669–14674, 2014.

[20] A.-K. Hatz, R. Calaminus, J. Feijoo et al., "Chemical stability and ionic conductivity of LGPS-type solid electrolyte Tetra-Li7SiPS8 after solvent treatment," *ACS Applied Energy Materials*, vol. 4, no. 9, pp. 9932–9943, 2021.

[21] F. Zheng, M. Kotobuki, S. Song, M. O. Lai, and L. Lu, "Review on solid electrolytes for all-solid-state lithium-ion batteries," *Journal of Power Sources*, vol. 389, pp. 198–213, 2018.

[22] W. Kohn and L. J. Sham, "Self-consistent equations including exchange and correlation effects," *Physical Review*, vol. 140, no. 4A, pp. A1133–A1138, 1965.

[23] B. J. Alder and T. E. Wainwright, "Studies in molecular dynamics," *The Journal of Chemical Physics*, vol. 31, pp. 459–466, 1959.

[24] J. Schmidt, M. R. G. Marques, S. Botti, and M. A. L. Marques, "Recent advances and applications of machine learning in solid-state materials science," *NPJ Computational Materials*, vol. 5, no. 1, p. 83, 2019.

[25] R. Jaafreh, Y. S. Kang, and K. Hamad, "Lattice thermal conductivity: an accelerated discovery guided by machine learning," *ACS Applied Materials & Interfaces*, vol. 13, no. 48, pp. 57204–57213, 2021.

[26] Y. Luo, M. Li, H. Yuan, H. Liu, and Y. Fang, "Predicting lattice thermal conductivity via machine learning: a mini review," *NPJ Computational Materials*, vol. 9, no. 1, p. 4, 2023.

[27] S. Ghosal, S. Chowdhury, and D. Jana, "Impressive thermoelectric figure of merit in two-dimensional tetragonal pnictogens: a combined first-principles and machine-learning approach," *ACS Applied Materials & Interfaces*, vol. 13, no. 49, pp. 59092–59103, 2021.

[28] S. Pereznieto, R. Jaafreh, J. Kim, and K. Hamad, "Solid electrolytes for Li-ion batteries via machine learning," *Materials Letters*, vol. 337, p. 133926, 2023.

[29] S. Kong, F. Ricci, D. Guevarra, J. B. Neaton, C. P. Gomes, and J. M. Gregoire, "Density of states prediction for materials discovery via contrastive learning from probabilistic embeddings," *Nature Communications*, vol. 13, no. 1, p. 949, 2022.

[30] Z. Chen, N. Andrejevic, T. Smidt et al., "Direct prediction of phonon density of states with Euclidean neural networks," *Advancement of Science*, vol. 8, no. 12, article 2004214, 2021.

[31] S. Muy, J. C. Bachman, L. Giordano et al., "Tuning mobility and stability of lithium ion conductors based on lattice dynamics," *Energy & Environmental Science*, vol. 11, no. 4, pp. 850–859, 2018.

[32] A. Einstein, "Die Plancksche Theorie der Strahlung und die Theorie der spezifischen Wärme," *Annalen der Physik*, vol. 327, no. 1, pp. 180–190, 1907.

[33] K. Wakamura, "Roles of phonon amplitude and low-energy optical phonons on superionic conduction," *Physical Review B*, vol. 56, no. 18, pp. 11593–11599, 1997.

[34] A. Jain, S. P. Ong, G. Hautier et al., "Commentary: the materials project: a materials genome approach to accelerating materials innovation," *APL Materials*, vol. 1, no. 1, article 011002, 2013.

[35] L. Ward, A. Agrawal, A. Choudhary, and C. Wolverton, "A general-purpose machine learning framework for predicting properties of inorganic materials," *NPJ Computational Materials*, vol. 2, no. 1, article 16028, 2016.

[36] L. Ward, R. Liu, A. Krishna et al., "Including crystal structure attributes in machine learning models of formation energies via Voronoi tessellations," *Physical Review B*, vol. 96, no. 2, article 24104, 2017.

[37] R. Jaafreh, Y. S. Kang, and K. Hamad, "Brittle and ductile characteristics of intermetallic compounds in magnesium alloys: a large-scale screening guided by machine learning," *Journal of Magnesium and Alloys*, vol. 11, no. 1, pp. 392–404, 2023.

[38] R. Jaafreh, T. Abuhmed, J.-G. Kim, and K. Hamad, "Crystal structure guided machine learning for the discovery and design of intrinsically hard materials," *Journal of Materiomics*, vol. 8, no. 3, pp. 678–684, 2022.

[39] R. Jaafreh, A. Sharan, M. Sajjad, N. Singh, and K. Hamad, "A machine learning-assisted approach to a rapid and reliable screening for mechanically stable perovskite-based materials," *Advanced Functional Materials*, vol. 33, no. 1, article 2210374, 2023.

[40] A. P. Bartók, R. Kondor, and G. Csányi, "On representing chemical environments," *Physical Review B*, vol. 87, no. 18, 2013.

[41] L. Himanen, M. O. J. Jager, E. V. Morooka et al., "DScribe: library of descriptors for machine learning in materials science," *Computer Physics Communications*, vol. 247, article 106949, 2020.

[42] M. Geiger and T. Smidt, "e3nn: Euclidean Neural Networks," 2022, https://arxiv.org/abs/2207.09453.

[43] S.-Y. Louis, Y. Zhao, A. Nasiri et al., "Graph convolutional neural networks with global attention for improved materials property prediction," *Physical Chemistry Chemical Physics*, vol. 22, no. 32, pp. 18141–18148, 2020.

[44] W. Pokojski and P. Pokojska, "Voronoi diagrams – inventor, method, applications," *Polish Cartographical Review*, vol. 50, no. 3, pp. 141–150, 2018.

[45] E. Wigner and F. Seitz, "On the constitution of metallic sodium," *Physical Review*, vol. 43, no. 10, pp. 804–810, 1933.

[46] S. B. Torrisi, M. R. Carbone, B. A. Rohr et al., "Random forest machine learning models for interpretable X-ray absorption near-edge structure spectrum-property relationships," *npj Computational Materials*, vol. 6, no. 1, p. 109, 2020.

[47] F. Yu, C. Wei, P. Deng, T. Peng, and X. Hu, "Deep exploration of random forest model boosts the interpretability of machine learning studies of complicated immune responses and lung burden of nanoparticles," *Science Advances*, vol. 7, article eabf4130, 2021.

[48] J. M. Barrios and P. E. Romero, "Decision tree methods for predicting surface roughness in fused deposition modeling parts," *Materials*, vol. 12, no. 16, p. 2574, 2019.

[49] N. Wagner and J. M. Rondinelli, "Theory-guided machine learning in materials science," *Frontiers in Materials*, vol. 3, 2016.

[50] M. de Jong, W. Chen, R. Notestine et al., "A statistical learning framework for materials science: application to elastic moduli of k-nary inorganic polycrystalline compounds," *Scientific Reports*, vol. 6, no. 1, p. 34256, 2016.

[51] S. Bates, T. Hastie, and R. Tibshirani, "Cross-validation: what does it estimate and how well does it do it?," *Journal of the American Statistical Association*, vol. 14, pp. 1–12, 2023.

[52] A. Botchkarev, "Performance Metrics (Error Measures) in Machine Learning Regression, Forecasting and Prognostics: Properties and Typology," 2018, https://arxiv.org/abs/1809.03006.

[53] A. Togo and I. Tanaka, "First principles phonon calculations in materials science," *Scripta Materialia*, vol. 108, pp. 1–5, 2015.

[54] S. Wang, Y. Zhang, X. Zhang et al., "High-conductivity argyrodite Li6PS5Cl solid electrolytes prepared via optimized sintering processes for all-solid-state lithium–sulfur batteries," *ACS Applied Materials & Interfaces*, vol. 10, no. 49, pp. 42279–42285, 2018.

[55] P. Vadhva, J. Hu, M. J. Johnson et al., "Electrochemical Impedance Spectroscopy for All-Solid-State Batteries: Theory Methods and Future Outlook," *ChemElectroChem*, vol. 8, no. 11, pp. 1930–1947, 2021.

[56] N. C. Rosero-Navarro, A. Miura, and K. Tadanaga, "Preparation of lithium ion conductive Li6PS5Cl solid electrolyte from solution for the fabrication of composite cathode of all-solid-state lithium battery," *Journal of Sol-Gel Science and Technology*, vol. 89, no. 1, pp. 303–309, 2019.

[57] K. Hikima, N. H. H. Phuc, H. Tsukasaki, S. Mori, H. Muto, and A. Matsuda, "High ionic conductivity of multivalent cation doped Li6PS5Cl solid electrolytes synthesized by mechanical milling," *RSC Advances*, vol. 10, no. 38, pp. 22304–22310, 2020.

[58] W. D. Jung, M. Jeon, S. S. Shin et al., "Functionalized sulfide solid electrolyte with air-stable and chemical-resistant oxysulfide nanolayer for all-solid-state batteries," *ACS Omega*, vol. 5, no. 40, pp. 26015–26022, 2020.

[59] K. Yamamoto, M. Takahashi, K. Ohara et al., "Synthesis of sulfide solid electrolytes through the liquid phase: optimization of the preparation conditions," *ACS Omega*, vol. 5, no. 40, pp. 26287–26294, 2020.

[60] P. Giannozzi, S. Baroni, N. Bonini et al., "QUANTUM ESPRESSO: a modular and open-source software project for quantum simulations of materials," *Journal of Physics Condensed Matter*, vol. 21, no. 39, 2009.

[61] A. Togo, "First-principles phonon calculations with Phonopy and Phono3py," *Journal of the Physical Society of Japan*, vol. 92, no. 1, article 012001, 2023.

[62] G. Kresse, J. Furthmuller, and J. Er, "Ab initioForce Constant Approach to Phonon Dispersion Relations of Diamond and Graphite," *Europhysics Letters*, vol. 32, no. 9, pp. 729–734, 1995.

[63] D. Alfè, "PHON: a program to calculate phonons using the small displacement method," *Computer Physics Communications*, vol. 180, no. 12, pp. 2622–2633, 2009.

[64] H. Jonsson, G. Mills, and K. W. Jacobsen, "Nudged elastic band method for finding minimum energy paths of transitions," in *Classical and Quantum Dynamics in Condensed Phase Simulations*, pp. 385–404, World Scientific, 1998.

[65] Y. Zheng, Y. Yao, J. Ou et al., "A review of composite solid-state electrolytes for lithium batteries: fundamentals, key materials and advanced structures," *Chemical Society Reviews*, vol. 49, no. 23, pp. 8790–8839, 2020.